PAPER

Check for updates

Enhancement of mechanical and energy storage properties of Ba(Ti$_{0.8}$Co$_{0.2}$)O$_3$ Pb-free ceramics by addition of Nd^{3+} ions

Saleh M. Matar,[ab] Elbadawy A. Kamoun, [ID] *[cd] Abd El-Razek Mahmoud,[e]
H. F. Mohamed, [ID] [f] A. M. Ahmed,[f] Gehad Mohamed Elhefnawy,[g] Ahmed I. Ali, [ID] *[hi]
Jong Yeog Son [ID] *[i] and Amr Ali[j]

Composites of (Ba$_{1-x}$Nd$_x$)(Ti$_{0.8}$Co$_{0.2}$)O$_3$ (abbreviated as BNTC) (x:0.1, 0.2 and 0.3 mol%) Pb-free ceramics were prepared through a conventional solid-state reaction method. The crystal structure, dielectric, magnetic susceptibility, mechanical and galvanostatic charging properties of prepared ceramics were investigated. A slight shift in diffraction peaks towards the higher angles along with variation in the crystal structure from the orthorhombic phase to the rhombohedral phase was observed with increasing Nd amounts. Significant enhancement in dielectric properties of BNTC was achieved by increasing the amount of Nd. The permittivity (ε_r) and phase transition temperature (T_m) increased from 3947 at 133 °C to 17 710 at 216 °C when the amount of Nd increased from 0.1 to 0.3. The magnetic results revealed that BNTC exhibited a ferromagnetic to paramagnetic phase transition at (T_c) due to the double exchange interaction in Nd^{3+}(Co^{3+})O^{2-}-Nd^{4+}(Co^{4+}) bonds. Whereas, antiferromagnetic to ferromagnetic phase transition was observed at (T_N) due to the super-exchange interaction in Nd^{3+}(Co^{3+})O^{2-}-Nd^{3+}(Co^{3+})/Nd^{4+}(Co^{4+})O^{2-}-Nd^{4+}(Co^{4+}). Further, the addition of Nd shows a significant enhancement in mechanical properties and elastic modulus, including Young's modulus (E), longitudinal modulus (L), shear modulus (G), and bulk modulus (K), due to the optimization of the structural properties. Superior enhancement in the charging/discharging time of BNTC ceramics was achieved by increasing the Nd content. The charging/discharging time decreased from 0.146 s to 0.007 s when the amount of Nd increased from 0.1 to 0.3. The present results indicate that the BNTC sample with Nd = 0.3 may be a promising ferromagnetic material for ultrafast charging.

[a] *Chemical Engineering Department, Faculty of Engineering, Jazan University, Jazan, 45142, Saudi Arabia*

[b] *Bioprocess Development Department, Genetic Engineering and Biotechnology Research Institute (GEBRI) City of Scientific Research and Technological Applications (SRTA-City), New Borg Al-Arab City, 21934, Alexandria, Egypt*

[c] *Department of Chemistry, College of Science, King Faisal University, Al-Ahsa, 31982, Saudi Arabia. E-mail: ekamoun@kfu.edu.sa*

[d] *Polymeric Materials Research Department, Advanced Technology and New Materials Research Institute (ATNMRI), City of Scientific Research and Technological Applications (SRTA-City) Alexandria, New Borg El-Arab City, 21934, Egypt*

[e] *Ferroelectric & Piezoelectric measurements Lab, Physics department, Faculty of Science, South Valley University, Qena, 83523, Egypt*

[f] *Physics Department, Faculty of Science, Sohag University, 82524 Sohag, Egypt*

[g] *Ultrasonic Metrology Department, National Institute of Standards, Giza, Egypt*

[h] *Basic Science Department, Faculty of Technology and Education, Helwan University, Saray–El Qoupa, El-Sawah Street, 11281, Cairo, Egypt*

[i] *Department of Applied Physics and Institute of Natural Sciences, College of Applied Science, Kyung Hee University, Suwon, 446-701, Republic of Korea. E-mail: jyson@khu.ac.kr*

[j] *Production Technology Department, Faculty of Technology & Education, Sohag University, 82524 Sohag, Egypt*

1. Introduction

The technology of advanced micro-electronics and communications industry required the development of materials science where dielectric capacitors impacted strongly in the applications, including hybrid electronic vehicles, telecommunication equipment and transportable electronics due to their excellent performance in high power density, service time and environmental friendliness,[1–3] The multiferroics are important for industrial applications.[4–6] It is important to find appropriate dielectric materials with high permittivity and high power density, such as BaTiO$_3$.[7–17] Composite ceramic materials with high dielectric constants have received extensive attention owing to their application in multilayer ceramic capacitors (MLCCs).[18–24]

Multiferroic materials have molecules that are electrified and magnetized in response to the application of external electric and magnetic fields. This occurs when magnetization and dielectric polarization are proportionate to the electric field and magnetic field, respectively,[25,26] Multiferroic materials exhibit at least two of the four states, including ferroelectricity

Paper

or antiferroelectricity, ferromagnetism or antiferromagnetism, and ferro-elasticity or ferro-torpidity.[27–31] These are useful for many advanced technological fields, such as optical communication, piezoelectrics, oxygen separation membranes, charge storage, sensors, and ferroelectric solar panels.[32–34] The piezoelectric response depends on several factors, such as electric polarization, crystal structure, fabrication method, intrinsic and extrinsic contributions of lattice motion, domain wall motion, and interphase boundary motion.[34,35]

A few single-phase materials are generally available with multiferroic properties and display a weak magnetoelectric coupling coefficient.[36] Their weak ferromagnetic, antiferromagnetic, and leaky ferroelectric characteristics motivated us to create multiferroic composites, which are used to provide improved material multiferroic properties. The technological industry requires composites with both ferromagnetic and ferroelectric phases and a critical temperature above room temperature,[37,38] One of the most eco-friendly systems is the $BaTiO_3$-based compositions. The majority of ferroelectric materials rely on the hybridization of occupied p-orbitals of the octahedrally coordinated oxygen ions with empty d-orbitals of transition metals to drive their ferroelectricity,[39,40] Due to its requirement for empty d-orbitals, this mechanism is unable to produce multiferroic behavior. Theoretically, certain rare-earth ions with partially filled f-orbitals can exhibit magnetic behavior.

Generally, the larger cation A is associated with alkaline or rare-earth cations, such as Ca^{2+}, Sr^{2+}, Ba^{2+}, Pb^{2+}, La^{3+}, Bi^{3+}, Pr^{3+}, and Ce^{3+}, permitting the dodecahedral coordination. Besides, the smaller cation B is associated with transition metal cations with octahedral coordination, such as Ti^{4+}, Zr^{4+}, $Mn^{3+/4+}$, Fe^{3+}, Co^{3+}, Cr^{3+}, and Ni^{3+}.[41–44] The properties of a material can be improved by substituting impurity ions into a lattice. $BaTiCoO_3$ (BTCO) is a material that can host a variety of dopant ions of different sizes because of its perovskite structure. To enhance the properties of BTCO, numerous researchers replaced the BTCO at the Ba site with trivalent ions such as La^{3+}, Nd^{3+}, or Sm^{3+} or divalent ions such as Ba^{2+}, Pb^{2+}, Sr^{2+}, or Ca^{2+} and the Co site with V^{5+}, Nb^{5+}, Mn^{4+}, Ti^{4+}, or Cr^{3+} ions. Enhancing the multifunctional characteristics of bulk and thin film BTCO also involves substituting rare earth ions like Gd^{3+}, La^{3+}, Dy^{3+}, Sm^{3+}, or Y^{3+}.[45–47] The influence of rare-earth Nd/Sm doping on the multiferroic and structural characteristics of $BiFeO_3$ ceramics made using spark plasma sintering has been studied. The crystal structure transitions from $R3c$ to co-existing $Pbam$ and $R3c$ when the Nd/Sm doping content rises above 10 mol%. Furthermore, the results demonstrate that Nd/Sm doping significantly reduces the grain size in all samples and improves their dielectric, ferroelectric, and magnetic characteristics.[48] Chchiyai et al. studied cobalt-doped lead titanate polycrystalline perovskites $PbTi_{1−x}Co_xO_{3−δ}$, which crystallized in the space group of the tetragonal perovskite structure. With an increase in the amount of Co, the dielectric constant at room temperature decreased. There was no phase transition from room temperature to 380 °C, but the dielectric constant and dielectric loss did increase with temperature.[32]

$BaTiO_3$ piezoelectric ceramics (piezoelectric coefficient of 241 pC $N^{−1}$) using DLP for 3D printing technology was investigated with a maximum bending strength of 57.9 MPa and a relative density of 94.2% and piezoelectric coefficient of 241 pC $N^{−1}$ at a poling electric voltage of 2 kV $mm^{−1}$.[49]

Tai et al. studied $Bi_{1−x}La_xFeO_3$–$BaTiO_3$ by adding two types of rare earth ions (La^{3+} and Sm^{3+}) with distinct ionic radii. Ferroelectricity and strain response are significantly improved by doping rare earth ions (La^{3+} and Sm^{3+}) because it increases the total number of activated domains and causes a larger Bi ion off-centering and displacement of B-site ions, coupled with a larger lattice deformation. Greater displacement of B-site ions, a stronger random field, and dielectric relaxation are all caused by the greater ionic radius difference between Sm^{3+} and Bi^{3+}. These effects culminate in a stronger intrinsic property response, which can only be stimulated by a sufficiently large electric field.[50]

In this work, the composite of $(Ba_{1−x}Nd_x)(Ti_{0.8}Co_{0.2})O_3$ was prepared through a conventional solid-state reaction method with different concentrations of Nd contents (Nd: 0.1, 0.2 and 0.3 mol%) to find a co-existence point between magnetic state and ferroelectric state. Nd^{3+} is selected to create an oxygen vacancy in the A-site of the BT lattice, which subsequently increases the cation disorder and forms a relaxor phase with a pseudo-cubic crystal structure. Furthermore, the Nd ions can be used as a sintering aid and decrease the sintering temperature due to their lower ionic radius. Structural, dielectric, magnetic and mechanical properties were measured and discussed well. Further, experimental data of galvanostatic charging curves for the three samples at room temperature are measured for commercial supercapacitors. Specific capacity was estimated from the charge/discharge curves.

2. Materials and methods

2.1. Materials

The row chemical powder of $BaCO_3$ (99.99 Sigma Aldrich), Nd_2O_3 (4N), TiO_2(3N), and Co_3O_4 (3N) were obtained from Sigma Aldrich, Germany. Other lab salts were obtained from (Al-Gomohouriya Co. LTD, Cairo, Egypt). Composites were grinded well for the $[(Ba_{1−x}Nd_x)(Ti_{0.8}Co_{0.2})]O_3$, ($x$ = 0.1, 0.2 and 0.3 mol%).

2.2. Preparation of composites

Lead-free composites with a formula of $[(Ba_{1−x}Nd_x)(Ti_{0.8}Co_{0.2})]O_3$, ($x$ = 0.1, 0.2 and 0.3 mol%) were prepared by the established solid-state reaction technique in air. High-purity fine-dried powders of $BaCO_3$, Nd_2O_3, TiO_2 and Co_3O_4 were weighted according to the chemical formula and mixed by ball milling (zirconia balls and ethanol for 24 h at room temperature). After milling, the mixed powders were dried in an oven at 80 °C for 4 h. The dried powders were sieved through 80 μm, then calcined at 1200 °C for 2 h in platinum crucibles to avoid any contamination or impurities during the thermal processing.[16] Afterwards, the calcined powder was pressed into pellets (10 mm in diameter and 1 mm in thickness) with polyvinyl alcohol as a binder, then sintered at 1375 °C for 2 h in air.

2.3. Characterization

The crystal structures of calcined powder and sintered ceramics were investigated by X-ray diffraction (XRD model: X'pert PANalytical, France) with 1.5405 Å of CuK_α radiation.

Functional groups of the composites were identified by using an FT-IR spectroscopy model (Hitachi 3140, Japan). FT-IR spectra were recorded in the range of 400–4000 cm^{-1} and were measured on samples in KBr pellets. To measure the dielectric properties, two sides of polished pellets were coated with Ag-paste and burned at 600 °C for 15 min. The dielectric constant and dielectric tangent loss (tan (δ)) of prepared samples were assessed at different frequencies (0.5, 1, 10, 100 and 100 kHz) at temperatures ranging from 25–350 °C via a computerized LCR meter (TH2826 LCR Meter 20 Hz–5 MHz). The AC susceptibility of the composites was measured over the temperature range of 100 to 400 K with an applied magnetic field of 250 µT and frequency of 0.3 kHz using the Barrington Instruments MS2/MS3 Susceptibility/Temperature system. Mechanical measurements were performed using an Ultrasonic flaw detector USN 60, Krautkramer. In this technique, the ultrasonic transducer generates high-frequency ultrasound energy, driven by a pulser (Ultrasonic flaw detector, USN 60, Krautkramer), that introduces and propagates in the form of waves inside the material. After that, it returns in the form of an electrical signal or echo on the screen of the device. From the time interval measured between two successive echoes and the thickness of the material, the experimental data of galvanostatic charging curves for the three samples at room temperature was obtained for commercial supercapacitors in the range of 1–1000 F (National Research Center, NRC, Dokki, Egypt).

3. Results and discussions

3.1. Crystal structure verification

Fig. 1(a) displays X-ray diffraction patterns of $(Ba_{1-x}Nd_x)(Ti_{0.8}Co_{0.2})O_3$ (x = 0.1, 0.2 and 0.3 mol%) calcined powder at 1200 °C/3 h. Pure perovskite structures are observed in all compositions without substantial impurity phases under the detection limit of XRD, indicating that Nd^{3+} ions were totally diffused effectively into the BTC lattice and formed a similar BTCN solid solution at ambient temperature. The diffraction peaks are completely indexed with the BaTiO$_3$ perovskite structure. No significant shift in diffraction patterns can be observed in the

whole range of 2-theta. Similar patterns have been detected for BTCNx sintered ceramics at 1375 °C/3 h, indicating the high thermal stability of the crystal structure of present compounds (Fig. 1b).

A slight shift in diffraction peaks near the higher angles is detected at high Nd amounts owing to the lower ionic radius of Nd^{3+} (1.27 Å, CN = 12) than Ba^{2+} (1.61 Å, CN = 12), decreasing the volume of the cell lattice and subsequently decreasing the particle size. To illustrate the impact of Nd addition on the crystal structure of BTC, the enlarged patterns of (200) diffraction peaks are displayed in Fig. 1(c). Along with the variation of the volume cell, the extended patterns show that the incorporation of Nd ions has a significant effect on the crystal structure of BTC ceramics. The crystal structure changed from the orthorhombic phase at Nd = 0.1 to the rhombohedral phase at Nd = 0.3, which signifies a decrease in lattice symmetry and an increase in the cation disorder.[51] This is attributed to the presence of soft ceramics at Nd = 0.3 due to substituting isovalence (Ba^{2+}) by tri-valence (Nd^{3+}) in the A-site of lattice, which might reduce the oxygen vacancy effect and enhance the dielectric properties. The Goldschmidt tolerance factor (τ) was computed to calculate the stability and packing of cations and anions in the perovskite crystal structure, as given in the following equation.[52]

$$\tau = \frac{R_A + R_O}{\sqrt{2}(R_B + R_O)} \tag{1}$$

R_A, R_B, and R_O represent the ionic radii of cations at A-sites, B-sites, and oxygen, respectively. The ionic radii of all ions in the A and B-sites were determined as Ba^{2+} (1.61Å, CN = 12), Nd^{3+} (1.27Å, CN = 12), Ti^{4+} (0.605Å, CN = 6) and Co^{4+} (0.53Å, CN = 6), O^{2-} (1.4 Å, CN = 6).[53] According to the above equation, when Ba^{2+} is replaced by Nd^{2+}, the τ value decreases from 1.0574 for pure BTC doped with 0.1 of Nd to 1.0333 at 0.3 of Nd ions. This reflects the compositions belonging to the ferromagnetic phase along with increasing the relaxer degree at a high content of Nd ions. This behavior indicates an increase in the cation disorder, which subsequently decreases the lattice symmetry of the BTC lattice.
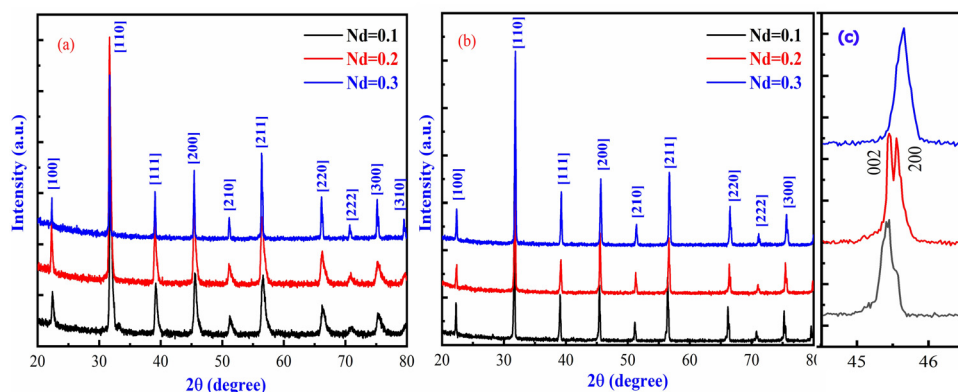

Fig. 1 X-ray diffraction patterns of the $(Ba_{1-x}Nd_x)(Ti_{0.8}Co_{0.2})O_3$ samples (x = 0.10, 0.20 and 0.30 mol%) (a) calcined powder at 1200 °C/3 h, (b) sintered ceramics at 1375 °C/3 h and (c) effect of Nd doping in the Nd$_x$Ba$_{1-x}$Ti$_{0.8}$Co$_{0.2}$O$_3$ composite.
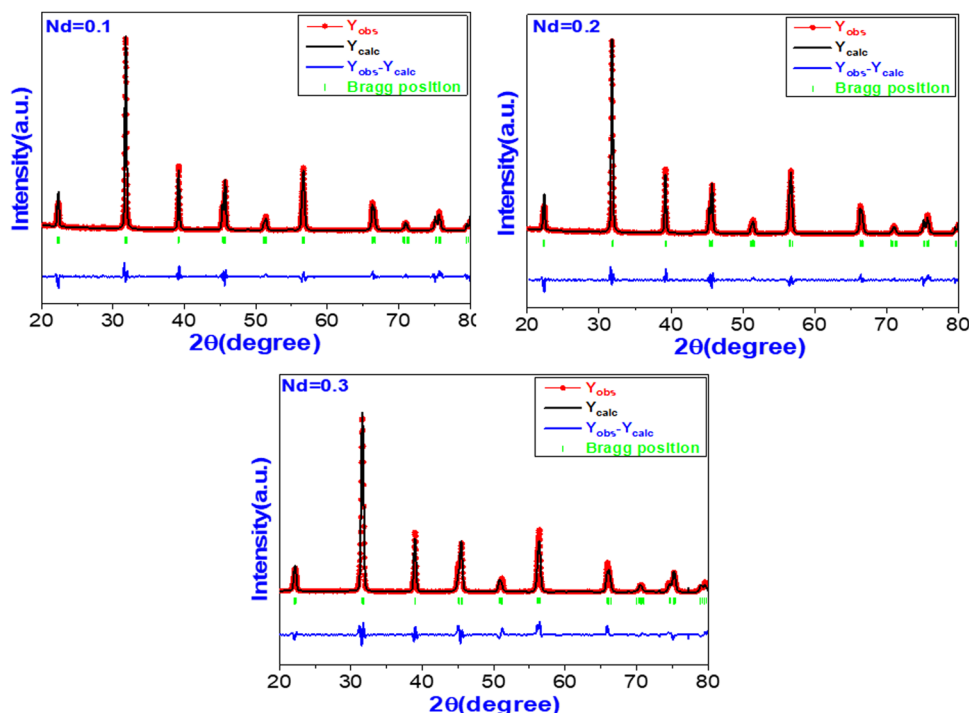
Fig. 2 Rietveld-refined XRD patterns of BNTC sintered ceramics.

To confirm the formation of the phases and structural development of the BNTC samples, we conducted Rietveld refinement utilizing the Full Prof software, allowing us to validate the obtained results. The refinement process employed an orthorhombic (*Amm2*-ICSD #01-081-2200) structure model and a rhombohedral (*R3m*-ICSD #01-086-1570) structure model. Fig. 2 illustrates the Rietveld-refined XRD patterns of the BNTC ceramics doped with glass. Table 1 provides the lattice parameters, direct cell volume and volume fraction corresponding to each phase. Similar results have been obtained by Essam *et al.*[54]

3.2. FT-IR spectroscopy

Fig. 3(a) shows the FT-IR of $(Ba_{1-x}Nd_x)(Ti0_{.8}Co_{0.2})O_3$ (x = 0.10, 0.20 and 0.30 mol%) composites. The FT-IR spectra of the composites agree with the standard spectrum of $BaTiO_3$. Herein, there are four absorption bands at 3416, 1628, 1432, 539 and 455 cm^{-1}. The absorption bands at 3416 and 1628 cm^{-1} are assigned to the presence of adsorbed moisture. The absorption band at 1432 cm^{-1} is due to the presence of some -OH groups on the surface of $BaTiO_3$ nano-crystallites. The absorption bands at 539 and 455 cm^{-1} are due to $BaTiO_3$. Consequently, the results indicated that the prepared composites at the high temperature

are completed at 1200 to 1300 °C. A deconvolution process was applied using a set of Gaussian functions to separate and determine the exact positions of the peaks and to disentangle overlapped peaks, as shown in Fig. 3(b). After applying the deconvolution process, distinct peaks were observed at 565, 661, 710, 820, and 905 cm^{-1} in the IR spectrum of the BNTC (Nd = 0.3) calcined powder. The peaks at 565 and 661 cm^{-1} are attributed to vibration modes of the Ti–O stretching in the Ti–O–Ti bridge connected with TiO_6. The peak at 710 cm^{-1} is attributed to the stretching vibration of Ti–O bonds in (TiO_6). The peak at 820 cm^{-1} is attributed to the stretching vibration of Ti–O bonds in (TiO_5). The peak at 905 cm^{-1} is attributed to the stretching vibration of Co–O bonds.[54]

3.3. Dielectric properties

Temperature-dependent dielectric constant (ε_r) and dielectric loss (tan δ) of $(Ba_{1-x}Nd_x)(Ti_{0.8}Co_{0.2})O_3$ (x = 0.1, 0.2 and 0.3 mol%) (BNTC) ceramics at altered frequencies (0.5, 1, 10, 100 and 1000 kHz) are explored in Fig. 4. It is worth noting that the ferroelectric phase is dependent on Nd-doping levels of 0.1 and 0.2, where the dielectric measurements are performed as a function of temperature with different applied electric fields (frequency). The Curie

Table 1 The values of the lattice parameters, direct cell volume and volume fraction (V_f) corresponding to each phase, orthorhombic (O), and rhombohedral (R)

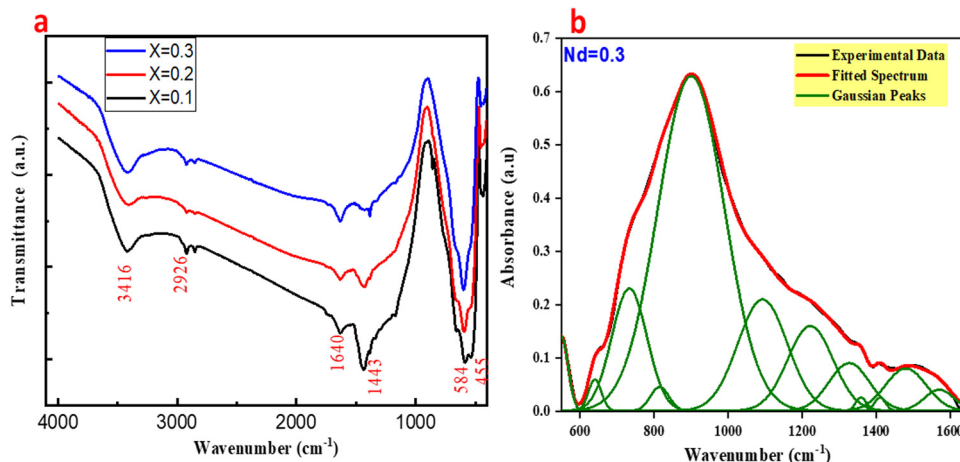|	O-phase					R-phase				
Sample code	a(Å)	b(Å)	c(Å)	V(Å³)	V_f %	a(Å)	b(Å)	c(Å)	V(Å³)	V_f %
0.1Nd	2.9165	4.8614	4.6010	65.234	100	00	00	00	00	00
0.2Nd	3.2184	4.8582	4.6047	71.975	80	3.008	3.008	3.008	27.68	20
0.3Nd	3.1557	4.8651	4.6016	70.6459	65.23	3.091	3.091	3.091	29.503	34.77

Fig. 3 (a) FT-IR spectra of BN$_x$TC samples (x = 0.10, 0.20 and 0.30 mol%); (b) deconvolution process for the IR spectrum for Nd = 0.3 calcined powder.

temperature corresponding to ferroelectric to paraelectric is independent of the applied frequency. This behavior confirms the tolerance factor values as mentioned above. Furthermore, enhancement of the dielectric constant of BNTC is achieved by the addition of Nd ions, which is attributed to the presence of soft ceramic materials, reducing the oxygen vacancy effect and increasing the cation disorder. The dielectric constant (ε) decreases as the applied frequency increases, which might be due to Deby's relaxer mechanism.[55] The composition with Nd ions = 0.3 shows different behavior compared to other ratios (0.1 and 0.2). The dielectric constant increases rapidly as the temperature increases and exhibits a maximum value at T_m (the temperature corresponding to maximum permittivity ε_m). Below T_m, the permittivity is strongly dependent on the frequency, while above T_m, the permittivity is frequency-independent, which indicates the presence

of a relaxer ferroelectric state. The present relaxer phase is due to the formed R-phase and decreases the τ value at room temperature. Significant enhancement in permittivity values and T_m are observed due to the presence of soft ceramic materials. On the other hand, the dielectric tangent loss of BNTC decreases as Nd content increases and is completely suppressed at Nd = 0.3, compared to the other compositions due to the reduction of the conduction, which is caused by the effect of oxygen vacancies.[56] The motive of the observed behavior is due to the free charges, which build up owing to the formation of defects. These defects occur due to the presence of oxygen vacancies in the A-site of the lattice during the synthesis of the material, intensifying the space charges on exposure to the external applied electric field. At a lower frequency, the charges acquire enough time to cover a greater path in the sample, causing a huge electronic polarization;
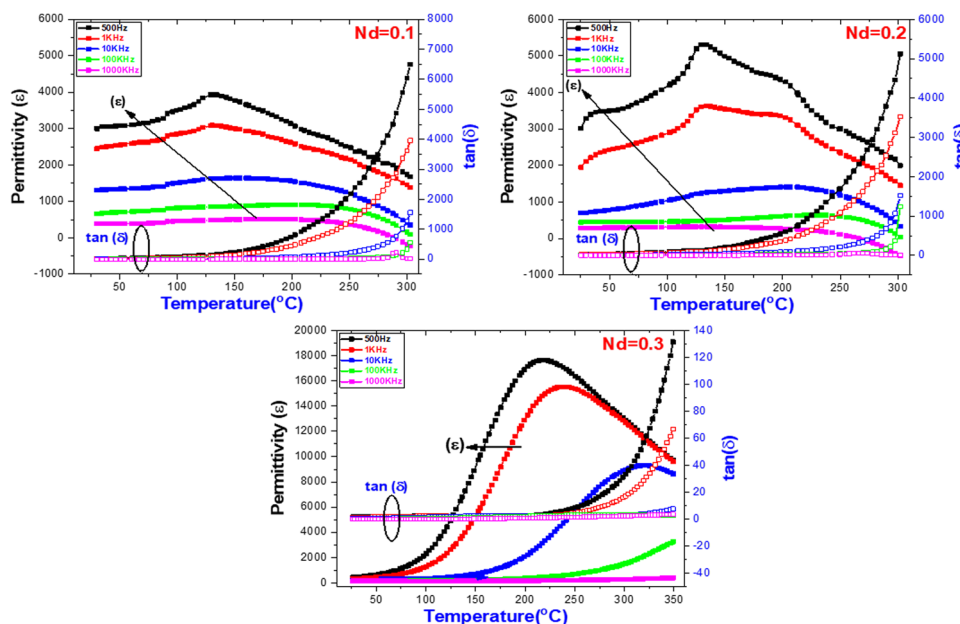

Fig. 4 Temperature dependence dielectric constant (ε_r) and dielectric tangent loss, tan (δ) of (Ba$_{1-x}$Nd$_x$)(Ti$_{0.8}$Co$_{0.2}$)O$_3$ composites (x = 0.10, 0.20 and 0.30 mol%).

hence, a greater value of ε' is obtained, as observed in all samples. With an increase in the value of frequency, the charge carriers lag to respond to the changing applied external field, and this results in a reduced polarizability in the material so that the permittivity decreases as the frequency increases.[55]

3.4. Magnetic susceptibility

The AC susceptibility of composites is measured over the temperature range of 100 to 400 K, with an applied magnetic field of 250 μT and frequency of 0.3 kHz. The dependence of the magnetic susceptibility on temperature (χ) is measured in a magnetic field of 300 A m^{-1}. Fig. 5 shows the (χ–T) curves for $(Ba_{1-x}Nd_x)$-$(Ti_{0.8}Co_{0.2})O_3$ composites (x = 0.10, 0.20 and 0.30 mol%). All samples exhibit an anti-ferromagnetic to ferromagnetic at a broad hump peak called (T_N) temperature. The T_N observed shifted to a higher temperature by increasing the amount of Nd. A sharp peak at a certain temperature called the Curie temperature (T_C) was detected, corresponding to the ferromagnetic to paramagnetic phase temperature (T_N).[57–59] The Curie temperature, T_C, is determined by extrapolating the inverse susceptibility $1/\chi$ in the high-temperature range to the temperature axis *via* the temperature curve.[60] The T_N and T_C values are calculated and presented in Table 2, where T_C is determined by the minimum of the dM/dT *versus* temperature curve, as shown in the inset in Fig. 5.

By doping $(Ba_{1-x}Nd_x)(Ti_{0.8}Co_{0.2})O_3$ samples with Nd ions (x = 0.10, 0.20 and 0.30 mol%), the magnetic moment and T_C values of composites increase. It can be interpreted that the occurrence of the antiferromagnetic super-exchange interaction in the $Nd^{3+}(Co^{3+})O^{2-}$–$Nd^{3+}(Co^{3+})/Nd^{4+}(Co^{4+})O^{2-}$–$Nd^{4+}(Co^{4+})$ bonds at low temperature is due to the ordering of the Co^{3+} spin state. The occurrence of the ferromagnetic interaction is due to the double exchange interaction in $Nd^{3+}(Co^{3+})O^{2-}$–$Nd^{4+}(Co^{4+})$ bonds.[60] The increase in magnetic moment and T_C value is attributed to hole doping with Ba^{2+} for Nd^{3+} ions and the creation of localized Co^{4+} ions, which enhances the double-exchange interaction.[61]

3.5. Mechanical properties

The Pulse Echo technique is the most stringent way of measuring the transient time in the material with ultrasonic waves.
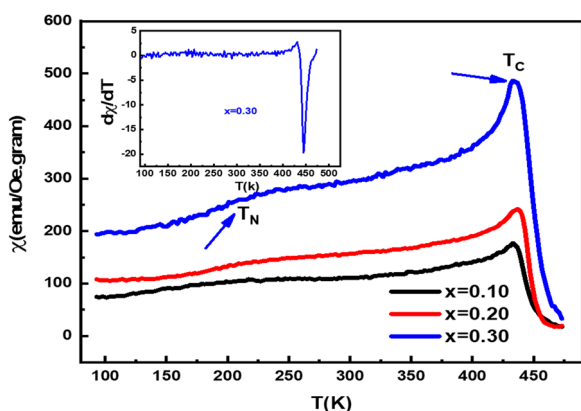

Fig. 5 Temperature dependence susceptibility of $(Ba_{1-x}Nd_x)(Ti_{0.8}Co_{0.2})O_3$ (x = 0.10, 0.20 and 0.30 mol%).

Table 2 The T_C and T_N values for the $(Ba_{1-x}Nd_x)(Ti_{0.8}Co_{0.2})O_3$ composites (x = 0.10, 0.20 and 0.30 mol%).samples (x = 0.10, 0.20 and 0.30 mol%)

Sample, x =	T_C (K)	T_N (K)
0.10	442	215
0.20	447	210
0.30	446	205

The velocity was measured from the following relationship:

$$V = \frac{2x}{\Delta t} \quad (2)$$

where, ample (2x) and Δt are the transient time interval between two successive echoes. Additionally, the densities of the prepared disks are calculated using the Archimedes method. Hence, the elastic modulus, Young's modulus E, longitudinal modulus L, shear modulus G, bulk modulus K and Poisson's ratio were calculated using the following relations (eqn (3)–(8)):

$$\rho = \rho_1(W_a/(W_a - W_1)) \quad (3)$$

$$E = \frac{[\rho \times V_S^2 \times (3 \times V_L^2 - 4 \times V_S^2)]}{(V_L^2 - V_S^2)} \quad (4)$$

$$L = \rho V_i^2 \quad (5)$$

$$G = \rho \times V_S^2 \quad (6)$$

$$K = L - (4/3)G \quad (7)$$

$$\nu = \frac{E}{2G} - 1 \quad (8)$$

ρ, ρ_l, W_a, W_l, V_L, V_S, are the sample density, liquid density, weight in air, weight in liquid, ultrasonic longitudinal wave velocity and shear wave velocity, respectively.[27–29] The molar volume was calculated from the atomic weight for this structure BNTC and is given in Table 3.

As depicted in Fig. 6(a), molar volume is inversely proportional to density. Herein, the addition of Nd is accompanied by the inhibition of grain growth of the disks. This is the reason behind the increase in the density from 5600.4 to 6349.9 kg cm^{-3}. Accordingly, the molar volume decreased from 42.1 to 37.4 cm^3 mol^{-1} as the Nd content increased from 0.1 to 0.3.[30–32]

Fig. 6(b) illustrates the relation between ultrasonic velocities *versus* Nd-contents.[33] As Nd increases, the values of the ultrasonic velocities rise. This behavior is attributed to the growing network dimensionality and connectivity, owing to the substitution of Nd ions on the A-site.[34] The increment in velocity and density results in an increase in the elastic modulus. Generally, the addition of Nd ions optimizes the elasticity of the ceramic material against pure BT with E around 115.5 GPa, as shown in Fig. 6(c),[35,36]

Fig. 6(c) shows the elastic modulus values of the prepared solid solution against different Nd contents. The elastic modulus, including Young's modulus E, longitudinal modulus L, shear modulus G, bulk modulus K and Poisson's ratio, as a function of Nd contents are shown in Fig. 6(c). All elastic

Table 3 Presents ultrasonic velocities, density, and accompanied elastic moduli for the prepared BT at different Nd ratios

Sample code parameter	S1	S2	S3
V_L (m s^{-1})	5998.6	6139.6	6531.8
V_S (m s^{-1})	3417.5	3600.6	3754.6
ρ (Kg m^{-3})	5600.4	6154.7	6349.9
$V_m \times 10^{-5}$ (m^3 mol^{-1})	42.1	38.4	37.4
E (GPa)	164.8	197.5	224.4
L (GPa)	201.5	232	270.9
G (GPa)	65.4	79.8	89.5
K (GPa)	114.3	125.6	151.6
ν	0.26	0.24	0.25

moduli increase with the Nd ion content in the compound $(Ba_{1-x}Nd_x)(Ti_{0.8}Co_{0.2})O_3$ composites (x = 0.10, 0.20 and 0.30 mol%). Here, replacing the Ba ions with Nd ions optimizes the elastic modulus, indicating a positive correlation between Nd ions doped in $Ba(Ti_{0.8}Co_{0.2})O_3$ and elastic modulus. Young's modulus E, longitudinal modulus L, shear modulus G, bulk modulus K and Poisson's ratio are given in Table 2. Noticeably, both the data in Table 2 and Fig. 6 confirmed that all elastic moduli were enhanced after the addition of rare earth elements (*i.e.*, neodymium).

3.6. Galvanostatic charging curves of supercapacitors

Fig. 7 presents the charge/discharge curves for three samples of $Nd_xBa_{1-x}Ti_{0.8}Co_{0.2}O_3$, where x = 0.10, 0.20 and 0.30 mol%. A symmetric, quarter rectangle, circle, and triangular shapes in their characteristics of a capacitive properties are found. Further, the steady spacing between peaks is indicative of high stabilities for all samples. Specific capacitance is calculated as the average value from a 1-cycle run using the discharge portion of the curve using eqn (9) and (10). The capacitance of the

supercapacitor (charged with applied constant current) can be determined from the slope of the voltage–time curve and is tabulated in Table 3.[61]

$$C = \frac{I}{\frac{dV}{dt}} \tag{9}$$

$$C_{sp} = \frac{4C}{m} \tag{10}$$

C is the capacitance of the whole cell, C_{sp} specific capacitance (Fig. 7), and m is the mass (g). By the built supercapacitor cells, experimental charge/discharge data curves were obtained by involving the PEEK cells in a Neware BTS4000 battery analyzer and controlling both voltage and current from their software. To collect data, measurement cycles were achieved to flush the electrodes with an electrolyte and ions that involved a short. To measure the data, cells are typically cycled between 0.15 and 0.6 V at a constant current of 11 mA g^{-1} constructed on active material mass.

Comparing the three samples, for the composite with Nd =0.3, the constructed electrodes released charge at a relatively high rate, which might be because of the lower surface area. This means that its full charge capacity was reached quickly (Table 4). A lower constant current of 0.011 A g^{-1} is essential to produce an equivalent charge/discharge curve, as using a constant current of 0.011 A g^{-1} gave a charge/discharge cycle time of about 2.5 s for the sample with Nd = 0.1. The sample doped with Nd = 0.2 is faster than the sample with Nd = 0.1, and the sample with Nd = 0.3 shows a triangle-like shape, which means it is faster for charging and discharging (Fig. 8) and (Table 4).
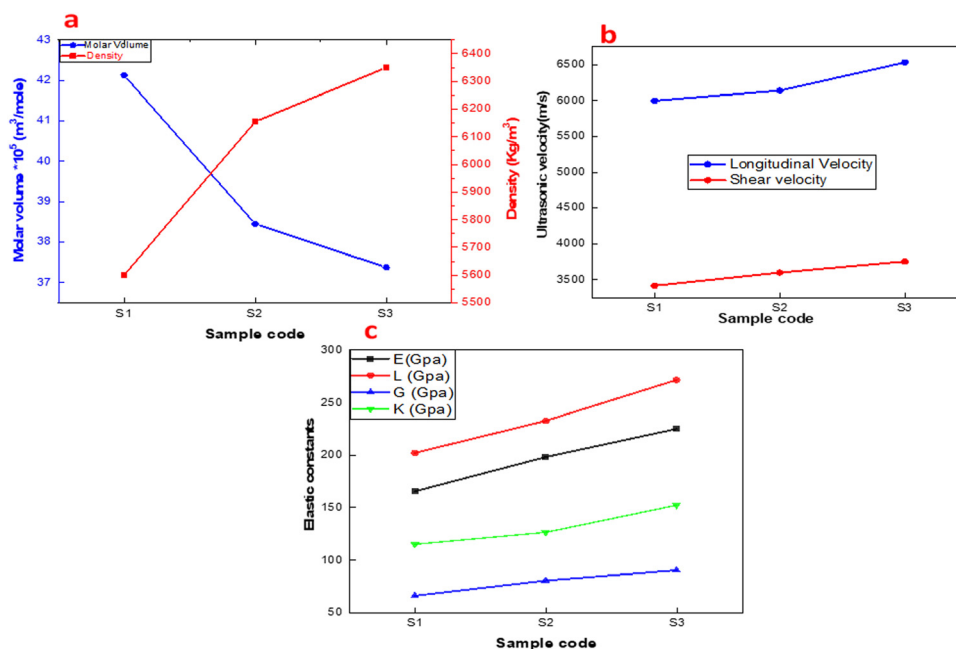

Fig. 6 (a) Molar volume and density (b) Longitudinal and shear velocities and (c) elastic modulus of $(Ba_{1-x}Nd_x)(Ti_{0.8}Co_{0.2})O_3$ composites (x = 0.10, 0.20 and 0.30 mol%).
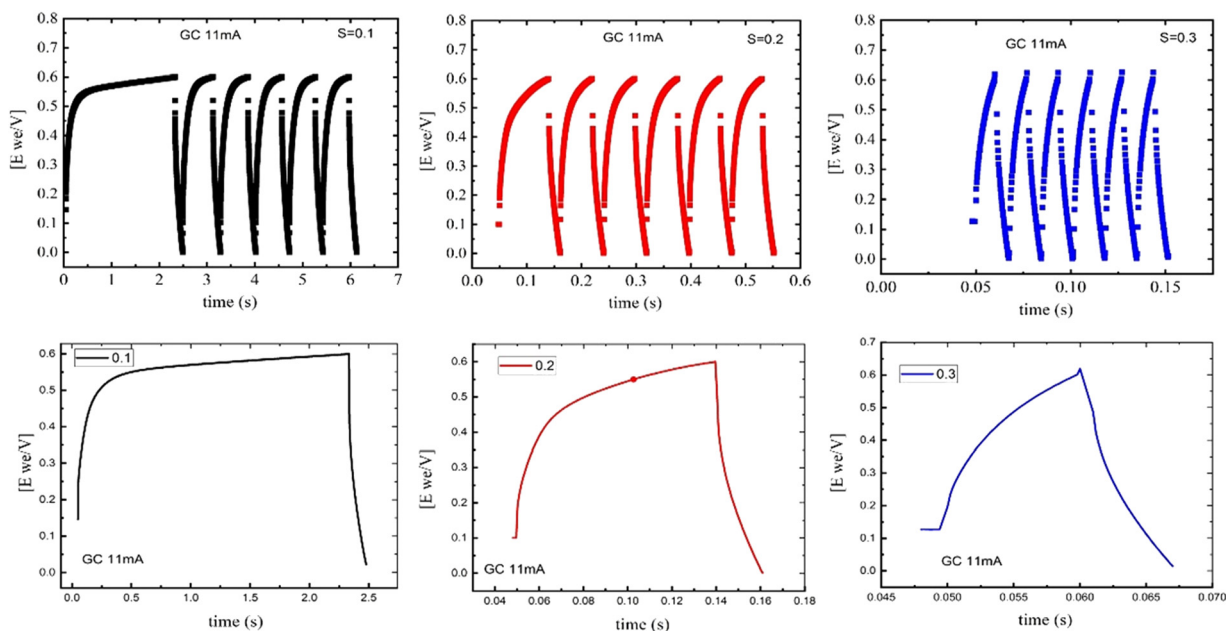
Fig. 7 The charge/discharge curves of $Nd_xBa_{1-x}Ti_{0.8}Co_{0.2}O_3$, where x = 0.10, 0.20 & 0.30 mol% supercapacitor at constant currents.

Table 4 Charge/discharge values of the time, potential, and specific capacity of $Nd_xBa_{1-x}Ti_{0.8}Co_{0.2}O_3$, where x = 0.10, 0.20 and 0.30 mol%, data calculated from the charge/discharge curves at constant currents

Current density	Discharge time (s)	Potential (V)	Specific capacity
0.011	0.146	0.5939	0.0027
0.011	0.022	0.5993	4.038×10^{-4}
0.011	0.007	0.4940	1.559×10^{-4}

4. Conclusions

Pb-free $(Ba_{1-x}Nd_x)(Ti_{0.8}Co_{0.2})O_3$ ceramics (x = 0.10, 0.20 and 0.30 mol%) were prepared through a conventional solid-state reaction method. Significant variation in crystal structure has been detected by the addition of Nd ions along with decreasing the tolerance factor from 1.0574 to 1.0333. Superior enhancement in dielectric properties was achieved by the addition of Nd

ions due to the formation of a soft ceramic material. The relaxor phase degree is enhanced in composition-dependent high content of Nd ions due to the high degree of cation disorder in the A-site of the lattice. The magnetic result data revealed the presence of a two-phase transition, corresponding to anti-ferromagnetic to ferromagnetic at T_N and then ferromagnetic to paramagnetic at T_C. Further, significant enhancement in the mechanical properties of BTC was achieved by the addition of Nd ions. The density increased from 5600.4 to 6349.9 g cm^{-3} and the molar volume decreased from 42.1 to 37.4 cm^3 mol^{-1} (as the Nd content increased from 0.1 to 0.3). The GCD results indicated an equivalent charge/discharge curve, with a constant current of 0.011 A g^{-1}, given a cycle time of about 2.5 s for the sample with Nd = 0.1. However, the composite with Nd = 0.2 is faster than the composite with Nd = 0.1, and the composite with Nd = 0.3 showed a triangle-like cycle, which means the charging and discharging are faster.

Author contributions:

Saleh Matar, A. E. Mahmoud and A. Ali: Experiments and data analysis; G. M. Elhefnawy, H. F. Mohamed, and A. M. Ahmed: characterized the samples, investigated the experimental results, contributed to an analysis of the data, A. E. Mahmoud, A. Ali and A. I. Ali writing the draft of the manuscript, and A. I. Ali, E. A. Kamoun and J. Y. Son: reviewing the final manuscript. All authors approved the final version of the manuscript for submission.

Ethical approval

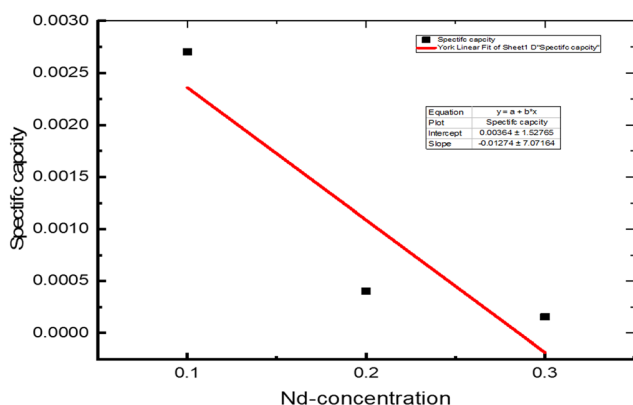No ethical approval was granted to conduct the experiments involved in the manuscript.

Fig. 8 Galvanostatic charge/discharge curves of the asymmetric capacitor at a constant current density of 11 mA.

Data availability

The data that support the findings of this study are available from the corresponding authors (E.A. Kamoun and J.Y. Son) upon reasonable request.

Conflicts of interest

The authors declare that no conflicts of interest exist that are relevant to the content of this article.

References

1 M. Balconi and A. Laboranti, University–industry interactions in applied research: The case of microelectronics, *Research Policy*, 2006, **35**(10), 1616–1630.

2 R. R. Tummala, E. J. Rymaszewski and A. G. Klopfenstein, *Microelectronics Packaging Handbook: Technology Drivers Part I*, 2012, Springer Science & Business Media.

3 O. Bonnaud, The technological challenges of microelectronics for the next generations of connected sensors, *Int. J. Plasma Environ. Sci. Technol.*, 2020, **14**(1), 1–8.

4 N. Imam, *et al.*, Optimization of magnetic properties of BaTiO$_3$/Li0. 5Fe$_2$. 5O$_4$ multiferroics prepared via modified low-temperature combustion, *J. Mater. Sci.: Mater. Electron.*, 2022, **33**(10), 7945–7959.

5 S. Dong, *et al.*, Multiferroic materials and magnetoelectric physics: symmetry, entanglement, excitation, and topology, *Adv. Phys.*, 2015, **64**(5–6), 519–626.

6 A. C. Lima *et al.*, *Magnetic materials for magnetoelectric coupling: An unexpected journey, in Handbook of Magnetic Materials*, 2020, Elsevier, pp. 57–110.

7 H. Tang, Y. Lin and H. A. Sodano, Synthesis of high aspect ratio BaTiO$_3$ nanowires for high energy density nanocomposite capacitors, *Adv. Energy Mater.*, 2013, **3**(4), 451–456.

8 A. E.-R. Mahmoud, *et al.*, Enhancement of switching/unswitching leakage current and ferroelectric properties appraised by PUND method of (Ba$_{1-x}$Ca$_x$)TiO$_3$ lead free piezoelectric near MPB, *Solid State Sci.*, 2019, **93**, 44–54, DOI: **10.1016/j.solidstatesciences.2019.04.011**.

9 A. I. Ali, C. W. Ahn and Y. S. Kim, Enhancement of piezoelectric and ferroelectric properties of BaTiO$_3$ ceramics by aluminum doping, *Ceram. Int.*, 2013, **39**(6), 6623–6629.

10 A. I. Ali, H. ElMeleegi and A. A. Moez, Investigation of structural, optical dielectrical and optical conductivity properties of BaTiO$_3$, Al0. 01Ba0. 99TiO$_3$ and La0. 01Ba0. 99TiO$_3$ thin films prepared by pulsed laser deposition, *Phys. Scr.*, 2019, **94**(12), 125810.

11 A. E.-r Mahmoud, *et al.*, Effect of domain switching contribution on polarization current, leakage current and switching charge density studied by PUND method in (Ba$_{1-x}$Ca$_x$)TiO$_3$ ceramics, *Mater. Sci. Eng., B*, 2019, **246**, 13–20, DOI: **10.1016/j.mseb.2019.05.022**.

12 A. I. Ali, *et al.*, Preparation, structural and dielectric properties of nanocomposite Al2O3/BaTiO$_3$ for multilayer ceramic capacitors applications, *J. Mater. Res. Technol.*, 2022, **18**, 2083–2092.

13 A. I. Ali, S. El-Sayed and A. Hassen, Change the ferroelectric properties of Al0.01Ba0.99TiO3 ceramics by Al0.01Sr0.99-TiO3 doping, *Results Phys.*, 2019, **14**, 102368.

14 M. M. Hussein., *et al.*, Structural and dielectric characterization of synthesized nano-BSTO/PVDF composites for smart sensor applications, *Mater. Adv.*, 2023, **4**, 5605–5617.

15 A. Er Mahmoud, S. Moeen and M. K. Gerges, Enhancing the tunability properties of pure (Ba,Sr)TiO3 lead-free ferroelectric by polar nanoregion contributions, *J. Mater. Sci.: Mater. Electron.*, 2021, **32**, 13248–13260, DOI: **10.1007/s10854-021-05879-616**.

16 A. I. Ali, C. W. Ahn and Y. S. Kim, Enhancement of piezoelectric and ferroelectric properties of BaTiO 3 ceramics by aluminum doping, *Ceram. Int.*, 2013, **39**(6), 6623–6629.

17 A. I. Ali and A. Hassen, Synthesis, characterization, ferroelectric, and piezoelectric properties of (1 − x)BaTiO$_3$−x(Ba-Ni$_{0.5}$Nb$_{0.5}$O$_3$) perovskite ceramics, *J. Mater. Sci.: Mater. Electron.*, 2021, **32**(8), 10769–10777.

18 A. M. Babeer, *et al.*, Moderation of [Bi3 +/Na1 +] molar ratio for enhancement of dielectric and energy storage properties of NaNbO3 ceramics, *Phys. Scr.*, 2024, **99**, 055901.

19 A. I. Ali and A. Hassen, Synthesis, characterization, ferroelectric, and piezoelectric properties of (1− x) BaTiO$_3$− x (BaNi$_{0.5}$Nb$_{0.5}$O$_3$) perovskite ceramics, *J. Mater. Sci.: Mater. Electron.*, 2021, **32**(8), 10769–10777.

20 M. Ezzeldien, A. M. Beagan, P. A. Alvi and A. Mahmoud, Effect of ZrO2 addition on the BO6 vibration modes of [(Bi$_{0.5}$Na$_{0.5}$)TiO$_3$ − SrTiO$_3$ − BaTiO$_3$] perovskite structure for enhancement energy storage properties, *Results Phys.*, 2024, **58**, 107445.

21 A. Er Mahmoud, A. A. Kamal and M. Ezzeldien, *et al.*, [Bi3 +/Zr4 +] induced ferroelectric to relaxor phase transition of BaTiO$_3$ ceramic for significant enhancement of energy storage properties and dielectric breakdown strength, *Appl. Phys. A*, 2024, **130**, 415, DOI: **10.1007/s00339-024-07417-7**.

22 A. I. Ali, *et al.*, Preparation, structural and dielectric properties of nanocomposite Al2O3/BaTiO$_3$ for multilayer ceramic capacitors applications, *J. Mater. Res. Technol.*, 2022, **18**, 2083–2092.

23 A. I. Ali, *et al.*, Ferroelectric, and piezoelectric properties of BaTi1-xAlxO3, $0 \le x \le 0.015$, *AIP Adv.*, 2015, **5**(9), 097125.

24 A. A. Moez, Y. Kim and A. I. Ali, Investigation of structure, optical, nonlinear optical, dielectrical properties and electronic results of La$_{0.01}$Ba$_{0.99}$TiO$_3$, Sm$_{0.5}$Sr$_{0.5}$CoO$_3$ and Sm$_{0.5}$Sr$_{0.5}$CoO$_3$/La$_{0.01}$Ba$_{0.99}$TiO$_3$ thin films grown on quartz substrates using pulsed laser deposition (PLD) technique, *J. Opt.*, 2021, **50**(2), 330–340.

25 D. Murzin, *et al.*, Ultrasensitive magnetic field sensors for biomedical applications, *Sensors*, 2020, **20**(6), 1569.

26 H. Schmid, Some symmetry aspects of ferroics and single phase multiferroics, *J. Phys.: Condens. Matter*, 2008, **20**(43), 434201.

27 D. Bochenek and P. Niemiec, Ferroelectromagnetic properties of PbFe1/2Nb1/2O3 (PFN) material synthesized by chemical-wet technology, *Materials*, 2018, **11**(12), 2504.

28 W. Eerenstein, N. Mathur and J. F. Scott, Multiferroic and magnetoelectric materials, *Nature*, 2006, **442**(7104), 759–765.

29 M. M. Vopson, Fundamentals of multiferroic materials and their possible applications, *Crit. Rev. Solid State Mater. Sci.*, 2015, **40**(4), 223–250.

30 T. Kimura, *et al.*, Magnetocapacitance effect in multiferroic BiMnO 3, *Phys. Rev. B: Condens. Matter Mater. Phys.*, 2003, **67**(18), 180401.

31 J. Scott, Multiferroic memories, *Nat. Mater.*, 2007, **6**(4), 256–257.

32 Z. Chchiyai, *et al.*, Effect of cobalt doping on the crystal structure, magnetic, dielectric, electrical and optical properties of $PbTi_{1-x}Co_xO_{3-\delta}$ perovskite materials, *J. Alloys Compd.*, 2022, **927**, 166979.

33 J. Huang, *et al.*, Enhanced mechanical properties and excellent electrical properties of PZT piezoelectric ceramics modified by YSZ, *Mater. Lett.*, 2022, **307**, 131006.

34 A. A. Kamal, *et al.*, Simultaneously enhanced of energy storage and energy harvesting performances of $[(Bi_{0.5}Na_{0.5})TiO_3–BaTiO_3]$ ceramics by addition of SrTiO3, *Phys. Scr.*, 2024, **99**, 055946.

35 J. Fu, *et al.*, Ultrahigh piezoelectricity in (Ba, Ca)(Ti, Sn) O3 lead-free compounds with enormous domain wall contribution, *Acta Mater.*, 2022, **230**, 117862.

36 P. E. Rubavathi, *et al.*, Enrichment of magnetoelectric effect in the hexagonal BaTi1-xCoxO3 artificial type-II multiferroics by defects, *J. Magn. Magn. Mater.*, 2021, **529**, 167927.

37 Y. Yin and Q. Li, A review on all-perovskite multiferroic tunnel junctions, *J. Materiomics*, 2017, **3**(4), 245–254.

38 S. Kumar, *Room-temperature spin-spiral multiferroicity in high-pressure cupric oxide*. 2013.

39 A. Aslla-Quispe, R. Miwa and J. Guerra, Role of the rare-earth doping on the multiferroic properties of $BaTiO_3$: First-principles calculation, *Physica B: Condensed Matter*, 2021, **615**, 413107.

40 A. I. Ali, A. Abdel Moez and Y. S. Kim, Hall mobility, electrical resistivity, and dielectric properties of reduced La 0.01 Ba 0.99 TiO 3, *J. Korean Phys. Soc.*, 2013, **62**, 1024–1030.

41 S. Rahman, *et al.*, Structural, electronic, optical and mechanical properties of oxide-based perovskite ABO3 (A= Cu, Nd and B= Sn, Sc): A DFT study, *J. Solid State Chem.*, 2023, **317**, 123650.

42 A. I. Ali, *et al.*, The influence of SrTiO 3 buffer layer on ferroelectric properties of Al-doped BaTiO 3 thin films, *J. Electroceram.*, 2014, **33**, 47–52.

43 A. I. Ali, *et al.*, Ferroelectric enhancement of La-doped $BaTiO_3$ thin films using $SrTiO_3$ buffer layer, *Thin Solid Films*, 2014, **551**, 127–130.

44 F. El Bachraoui, *et al.*, Unusual superparamagnetic behavior in bulk $Ba_{0.198}La_{0.784}Ti_{0.096}Fe_{0.8}O_{3-\delta}$, *Mater. Res. Bull.*, 2021, **137**, 111187.

45 G. M. A. Elhefnawy, *et al.*, Improvement of the structural, dielectric, ferroelectric, and piezoelectric of $PbZr_{0.52}Ti_{0.48}O_3$ nanopowder features for ultrasonic applications, *Ferroelectrics*, 2023, **615**(1), 8–28.

46 M. El-Gazery, A. Ali and R. El-Mallawany, Ultrasonic and thermal properties of bismuth borotellurite glasses doped with NdCl3, *Egypt. J. Chem.*, 2019, **62**(4), 655–664.

47 X. Yi, *et al.*, Resistive Switching Phenomenon for Flexible and Stretchable Memories, *in Flexible and Stretchable Electronics*, 2019, Jenny Stanford Publishing, pp. 114–156.

48 T. Wang, *et al.*, Effect of rare-earth Nd/Sm doping on the structural and multiferroic properties of BiFeO3 ceramics prepared by spark plasma sintering, *Ceram. Int.*, 2020, **46**(10), 15228–15235.

49 Z. Jiang, *et al.*, 3D printing of porous scaffolds $BaTiO_3BaTiO_3$ piezoelectric ceramics and regulation of their mechanical and electrical properties, *Ceram. Int.*, 2022, **48**(5), 6477–6487.

50 D. Tai, *et al.*, $BiFeO_3$-$BaTiO_3$ ferroelectrics: Decrypting the mechanism of rare earth doping-induced electrical property discrepancy via scaling behavior and multi-level structure, *Acta Mater.*, 2024, **262**, 119411.

51 A. E.-r Mahmoud, A. S. Afify and S. Parashar, Dielectric, tunability, leakage current, and ferroelectric properties of (K 0.45 Na 0.55) 0.95 Li 0.05 NbO 3 lead free piezoelectric, *J. Mater. Sci.: Mater. Electron.*, 2019, **30**, 2659–2668.

52 A. A. Kamal, *et al.*, The effect of domain switching on the lattice symmetry and dielectric properties of $(Bi_{0.5}Na_{0.3}K_{0.2})TiO_3$-0.2 $SrTiO_3$-$(Ba_{0.8}Ca_{0.2})$ TiO_3 piezo-ceramic by poling field, *Mater. Chem. Phys.*, 2022, **288**, 126420.

53 A. M. Babeer and A. E.-r Mahmoud, Suppression of the ferroelectric phase for $(K_{0.5}Na_{0.5})$ NbO3 ceramic by A/B-sites disorder for enhancement the energy storage properties and dielectric breakdown strength, *Mater. Today Commun.*, 2023, **36**, 106606.

54 E. A. Elkelany., *et al.*, New insights into the effect of glass addition on the piezoelectric and thermal stability properties of $(Ba_{0.85}Ca_{0.15})(Ti_{0.9}Zr_{0.1})O_3$Pb-free ceramic by defect engineering of MPB, *Ceram. Int.*, 2023, **49**, 38305–38317.

55 K. L. Routray and S. Saha, Graphene nanoplatelets anchored into Ag doped spinel $CoFe_2O_4$ nanohybrid: Synthesis, structural, electrical, superior dielectric and room temperature induced ferromagnetism performance for high frequency device application, *Diamond Relat. Mater.*, 2024, **141**, 110680.

56 P. Ren, *et al.*, Effects of doping sites on electrical properties of yttrium doped $BaTiO_3$, *Mater. Lett.*, 2016, **174**, 197–200.

57 S. Kolesnik, *et al.*, Comparison of magnetic and thermoelectric properties of (Nd, Ca) BaCo2O5.5 and (Nd, Ca) CoO3, *J. Appl. Phys.*, 2012, **111**(7), 07D727.

58 A. Ahmed, *et al.*, Thermopower and magnetocaloric properties in NdSrMnO/CrO3 composites, *J. Magn. Magn. Mater.*, 2018, **456**, 217–222.

59 P. Dutta, *et al.*, Effect of Co doping on magneto-transport properties of Eu0. 5Sr0. 5MnO3, *J. Alloys Compd.*, 2014, **590**, 313–317.

60 H. Mohamed, *et al.*, Impact of aluminum on the Seebeck coefficient and magnetic properties of $La_{0.7}Ba_{0.3}MnO_3$ manganites, *Chem. Phys. Lett.*, 2019, **726**, 22–28.

61 A. Ali, *et al.*, Magnetic phase transition and variable range hopping conduction of $Y_{1-x}Sr_xCoO_{3-\delta}$, *J. Korean Phys. Soc.*, 2007, **51**(5), 1736–1742.